

Facile Solvothermal Method for Fabricating Arrays of Vertically Oriented α -Fe₂O₃ Nanowires and Their Application in Photoelectrochemical Water Oxidation

Dong-Dong Qin,[†] Chun-Lan Tao,[‡] Su-il In,[§] Zheng-Yin Yang,^{*,†} Thomas E. Mallouk,[§] Ningzhong Bao,^{||} and Craig A. Grimes^{*,||}

[†]College of Chemistry and Chemical Engineering, State Key Laboratory of Applied Organic Chemistry, and [‡]School of Physical Science and Technology, Lanzhou University, Lanzhou 730000, People's Republic of China

[§]Department of Chemistry, The Pennsylvania State University, University Park, Pennsylvania 16802, United States

^{||}State Key Laboratory of Materials-Oriented Chemical Engineering, Nanjing University of Technology, Nanjing, Jiangsu 210009, People's Republic of China

ABSTRACT: The controlled growth of highly ordered, [211]-oriented FeOOH nanowire arrays on various substrates, such as Pt, W, Ti, and fluoride-doped tin oxide (FTO) glass, was achieved by a solvothermal method in aqueous acetonitrile solutions at 80–120 °C, following by annealing to form α -Fe₂O₃ nanowires with their [110] direction perpendicular to the substrate. Adjusting the reaction pH and temperature enables control of the nanowire length. In particular, the pH has a dramatic effect on the nanowire growth, with low pH resulting in the growth of longer wires because of the acid-catalyzed hydrolysis of acetonitrile. Photoactive hematite was prepared by diffusing Ti or Sn into the nanowires during thermal annealing. Processing parameters that influenced the photoelectrochemical performance of these nanowire arrays, including the annealing regime, temperature, and length of nanowires, are discussed in detail. The Ti- and Sn-doped one-dimensional [110]-oriented α -Fe₂O₃ nanowire arrays provide an effective pathway for electron transport, demonstrating increased photocurrents, up to 1.3 mA/cm² under air mass 1.5 global (AM 1.5G) illumination, in photoelectrochemical water oxidation.

INTRODUCTION

The photoelectrochemical conversion of solar to chemical energy using semiconductor electrodes has been a topic of great interest for several decades, offering the possibility of efficiently producing hydrogen from water by water photoelectrolysis.^{1–3} Among the most studied electrode materials, which include TiO₂, WO₃, and α -Fe₂O₃, hematite (α -Fe₂O₃) is one of the most promising oxides⁴ because it is inexpensive, environmentally benign, stable over a broad range of pH values, and composed of terrestrially abundant elements. Its band gap of 2.1 eV makes it possible for hematite to absorb roughly 38% of solar photons under air mass 1.5 global (AM 1.5G) conditions, and it is particularly interesting for tandem two band gap systems.⁵ However, the reported efficiencies for hematite photoelectrodes remain relatively low because of several factors that include fast recombination of photogenerated charge carriers,⁶ a short diffusion length for holes (2–4 nm),⁷ a low hole mobility (at room temperature) of ~ 0.01 cm² V^{−1} s^{−1},⁸ slow oxygen evolution reaction kinetics,⁹ a low flat band potential, and a significant reduction in the absorption cross-section for wavelengths approaching the band gap value. Substantial improvement in the photocurrent density of hematite has been achieved through morphological modifications and impurity doping.¹⁰ For example, cauliflower-like structured hematite¹¹ with an incident photon current efficiency (IPCE) of 42% at 370 nm at 1.23 V_{RHE} has been reported. Highly photoactive mesoporous hematite films^{12,13} and nanobelt-based hematite heteronanostructures¹⁴ have been successfully fabricated. Recently,

the fabrication of mesoporous hematite films through transformation of magnetite to hematite was reported.¹⁵ Quasi-one-dimensional α -Fe₂O₃ structures, such as wires, tubes, belts, and rods, are being increasingly studied for water photoelectrolysis because they combine efficient charge transfer with a high surface area that is readily accessible to electrolyte percolation. A number of methods, including templating,¹⁶ sol–gel synthesis,¹⁷ gas–solid reactions,¹⁸ hydrothermal crystallization,¹⁹ anodic oxidation,^{20,21} thermal processing of pure iron foil,²² and template-accelerated hydrolysis,²³ have been developed to synthesize one-dimensional (1D) α -Fe₂O₃ nanostructures.

The most common and effective strategy for making α -Fe₂O₃ (or β -FeOOH, followed by annealing for conversion to α -Fe₂O₃) nanostructures is the forced hydrolysis of Fe³⁺-containing solutions, but in most cases, this method requires extended reaction times. For example, Morales et al.²⁴ and Musić et al.²⁵ reported that more than 7 days are needed to grow α -Fe₂O₃ at 100 °C. Vayssieres et al.²⁶ were the first to synthesize β -FeOOH nanorod arrays on fluoride-doped tin oxide (FTO) substrates in a shorter time (24 h) through a hydrolysis–condensation approach from aqueous Fe³⁺ solutions. Peng et al.²⁷ later made β -FeOOH nanorod arrays by a hydrothermal modification of that method, but a reaction time of 24 h was still needed. The β -FeOOH nanorod arrays were transformed to [110]-oriented hematite by annealing at 500 °C.

Received: September 10, 2011

Revised: October 17, 2011

Published: October 17, 2011

Ling and co-workers²⁸ then successfully converted β -FeOOH nanorods to photoactive α -Fe₂O₃ by diffusing Sn from the FTO substrate by high-temperature annealing, motivated by the report from Sivula et al.¹² of Sn doping of mesoporous hematite films.

As a means of fabricating photoelectrodes suitable for efficient water photoelectrolysis, it is important to develop a convenient synthetic route to [110]-oriented crystalline hematite rods on suitable substrates that can be doped by rapid thermal processing. To that end, we report herein the fabrication of highly ordered, vertically oriented α -Fe₂O₃ nanowire arrays on various substrates by the combined action of a rapid low-temperature solvothermal technique in combination with annealing. This rapid solvothermal synthesis method minimizes processing costs and is environmentally friendly. Acetonitrile was found to be essential to growing uniform nanowire arrays in this process. Interestingly, the as-prepared [211] FeOOH nanowires are found to have a substructure, in which each wire consists of bundles of rods. The hematite nanowire films are doped by, respectively, the diffusion of Ti and Sn from the Ti foil and FTO substrates through high-temperature annealing.¹² The effects of the temperature, wire length, grain boundaries, and presence of a seed layer on the photoelectrochemical behavior of the nanowire arrays grown on FTO are detailed.

EXPERIMENTAL SECTION

Fabrication of the nanowire array films was as follows: 0.1 M FeCl₃ and 1.0 M NaNO₃ were dissolved in a 10 mL solution of x vol % (where $x = 0.5, 1, 1.5$, and 2 , corresponding to pH values of 1.55, 1.16, 0.99, and 0.9, respectively) HCl (36.5–38%) and acetonitrile in a volume ratio of 3:7. This solution was transferred to a Teflon-lined autoclave of 23 mL capacity, and a slide of FTO glass was loaded into the autoclave, which was then placed within an oven maintained at 80–120 °C for 4 h. The reactor was allowed to cool to ambient temperature, after which the sample was rinsed with deionized (DI) water and then blown dry with N₂. Samples were annealed at 650, 750, 800, and 820 °C in an oven (Lindberg/Blue) for 20 min in air with a ramp rate of 10 °C/min for both heating and cooling. Hematite seed layers were formed on the FTO-coated glass by spin coating (4000 rpm for 30 s) a solution comprised of 0.3 M FeCl₃, 5 wt % polyvinyl alcohol (PVA; $M_w = 89\,000$ – $98\,000$), and 0.3 wt % HCl (36.5–38%), which was then annealed at 500 °C in air for 2 h.

Sample morphology was imaged by use of a field-emission scanning electron microscope (FE-SEM; JSM6700F, JEOL, Japan). Transmission electron microscopy (TEM) and selected area electron diffraction (SAED) were performed using a Phillips EM 420 microscope. X-ray diffraction (XRD) patterns were measured on a Scintag X2 diffractometer using Cu K α radiation ($\lambda = 1.5418$ Å). Diffuse reflectance ultraviolet–visible (UV–vis) spectroscopy was recorded with a Perkin-Elmer Lambda 950 spectrophotometer. Linear sweep voltammetry was obtained at a scan rate of 20 mV/s using a BAS 100B electrochemical workstation. Photoelectrochemical properties were investigated using a three-electrode configuration with a hematite film as the working photoelectrode, Ag/AgCl as the reference electrode, and platinum foil as the counter electrode in 1 M NaOH. Sunlight was simulated with a 300 W xenon lamp (Spectra Physics) and an AM 1.5G filter (Oriol). The light intensity was set using a National Renewable Energy Laboratory (NREL) calibrated crystalline silicon solar cell. Electrochemical impedance spectroscopy (EIS) was performed using a Solartron 1260 impedance/gain-phase analyzer, with the data fit to an equivalent circuit model using ZView software. The superimposed alternating current (AC) signal was maintained at 10 mV, while the frequency was scanned between 100 kHz and 0.1 Hz at potentials between -0.3 and 0.3 V

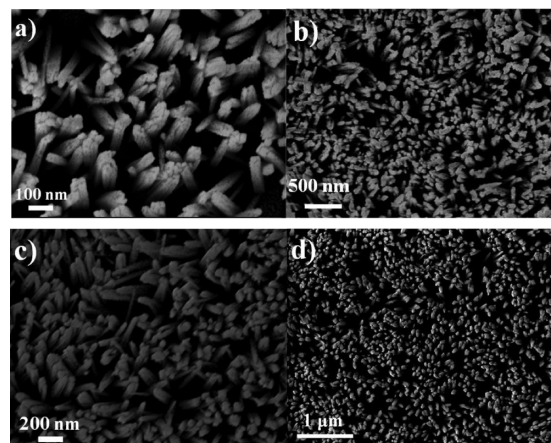


Figure 1. FE-SEM images of as-prepared nanowire arrays on (a) Pt (with a seed layer used to initiate growth), (b) W, (c) Ti, and (d) FTO-coated glass.

versus Ag/AgCl in the dark and under illumination in an electrolyte of 1 M NaOH, with Pt as the counter electrode. The capacitance was extracted from the EIS spectra by use of an equivalent circuit $R_s(CPE - R_p)$, where R_s is the ohmic contribution, CPE is the constant phase element that takes into account non-idealities in the capacitance of the Helmholtz layer, and R_p is the charge-transfer resistance. IPCE was measured using light from a 300 W xenon lamp (Spectra Physics) that was focused by a parabolic reflector and passed through a monochromator, at 0.5 V direct current (DC) bias. Samples were measured using a hematite film as the working photoelectrode and platinum foil as the counter electrode in 1 M NaOH.

RESULTS AND DISCUSSION

Panels a–d of Figure 1 show vertically aligned as-prepared nanowire array films obtained from a 70% acetonitrile solution on Pt (with use of a hematite seed layer), W, Ti, and FTO substrates, respectively. It can be seen that the wires are highly oriented and uniform in length, with no evident debris or broken wires on the top surface of the film, especially wires grown on FTO. The wires can be grown directly on W, Ti, and FTO substrates without use of a seed layer, which is necessary for nanowire growth on Pt. Acetonitrile proved to be a critical ingredient in the growth of FeOOH nanowire array films. If a 100% aqueous solution was used, only a densely packed film was obtained.

The nanowires grown on FTO have a diameter of 30–40 nm at the tip and 100–110 nm at the bottom. To avoid contact of the electrolyte with FTO in photoelectrochemical use, a seed layer was first deposited on the FTO substrate, which did not affect the diameter or length of the resulting nanowires. At pH 1.16, the length of the wires increased gradually with an increasing solvothermal temperature, as a result of we believe the accelerated hydrolysis of Fe³⁺, from 420 nm at 80 °C to 840 nm at 100 °C to 1.6 μ m at 120 °C. The pH significantly affected nanowire growth, with a tendency toward longer wires under lower pH solvothermal conditions. The pH and solvent effects can be explained by the acid-catalyzed hydrolysis of acetonitrile under solvothermal conditions. The hydrolysis reaction produces acetamide and acetic acid, which appear to play an important role in crystal growth. The formation of acetamide,²⁹ acetamide–metal complexes, and ammine–metal complexes plus acetic acid³⁰ in the presence of metal ions has been confirmed by Raman spectroscopy

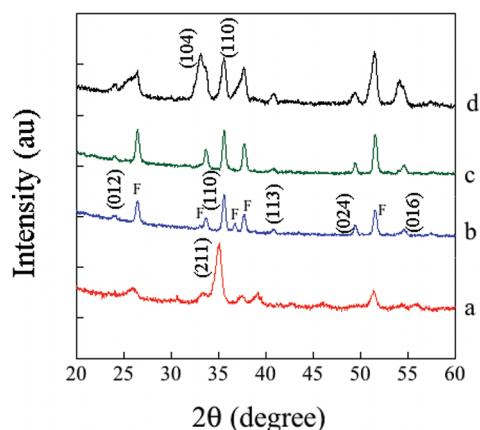


Figure 2. XRD patterns of 2.5 μm long hematite nanowire array films on FTO: (a) as prepared, (b) after a two-step 500/820 $^{\circ}\text{C}$ anneal, (c) after a 820 $^{\circ}\text{C}$ anneal, and (d) data from a 500 $^{\circ}\text{C}$ annealed nanoparticle hematite film.

and modeling the kinetics of acetonitrile hydrolysis. Similar effects have recently been reported for the hydrolysis of *N,N*-dimethylformamide under acidic conditions in the formation of nanostructured titanium oxide.³¹ When acetonitrile was replaced by ethanol, film thickness remained the same (1.2 μm) as the pH was varied between 1.55, 1.16, and 0.99. When the pH was lowered to 0.9, the thickness decreased markedly, to no more than 100 nm.

In summary, acetonitrile promotes the growth of nanowire array films several micrometers in length that are strongly adhered to the substrate under low pH conditions, low temperatures, and short reaction times. As-prepared nanowire arrays on FTO were confirmed to be FeOOH (JCPDS card number 75-1594) by XRD patterns, as shown in Figure 2. Pure hematite ($\alpha\text{-Fe}_2\text{O}_3$) was observed after annealing at temperatures above 500 $^{\circ}\text{C}$ (JCPDS card number 98-000-0240). No other crystalline phase was present. This result is consistent with those of previous studies in which $\beta\text{-FeOOH}$ was observed in as-prepared samples and hematite was obtained by subsequent annealing,^{26–28} but in the present method, a reaction time of only 4 h was needed to grow 2.5 μm wires. The use of acetonitrile in acidic solutions is a key to accelerating nanowire growth. The strongest peak in the XRD patterns, assigned as (211), indicates the preferred growth direction of the as-prepared FeOOH nanowire arrays. After annealing at 820 $^{\circ}\text{C}$, the thermally stable phase (hematite) was obtained with one dominant (110) reflection and several weak reflections corresponding to the (012), (113), (116), and (024) planes. The persistence of the dominant (110) peak implies that the nanowires retain their orientation upon annealing, a finding supported by FE-SEM images. The [110] direction provides an excellent path for diffusion of electrons because of the strongly anisotropic conductivity of hematite. Conduction in hematite, which follows a site hopping mechanism, is 4 orders of magnitude lower along the [001] direction than it is in the perpendicular (100) plane, which contains the [110] direction.³² Two dominant peaks (104) and (110) can be seen in nanoparticle films made by dip coating, which suggests the existence of multiple orientations and grain boundaries in nanostructures composed of these nanoparticles. TEM images reveal that the as-prepared FeOOH nanowires consist of bundles of rods and that the component rods are approximately 5 nm in diameter, as observed by Vayssieres et al.²⁶

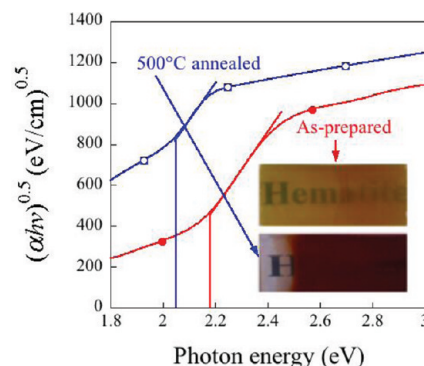


Figure 3. Optical spectra of as-prepared and annealed nanowire array films. Inset is a photograph of as-prepared and annealed nanowire arrays.

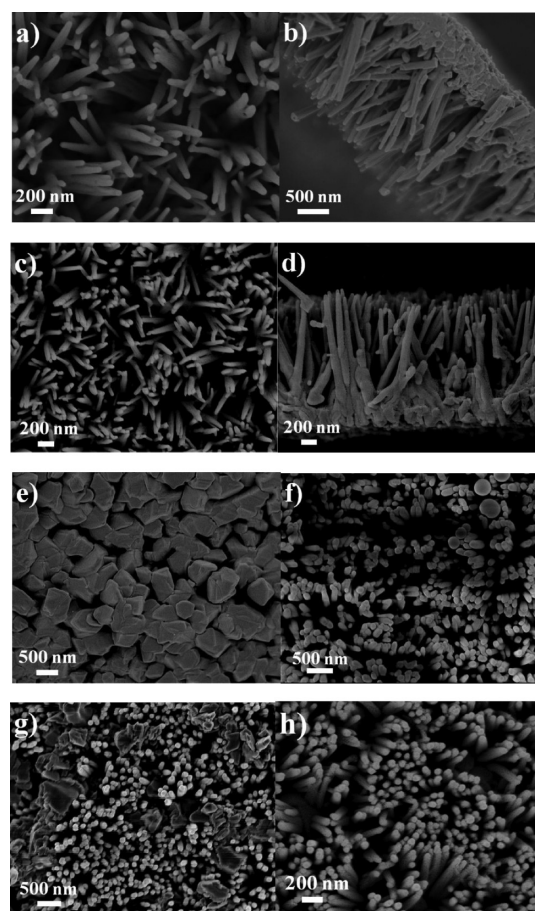


Figure 4. FE-SEM images of hematite nanowire arrays on Ti foil: (a and b) annealed at 500 $^{\circ}\text{C}$, (c and d) annealed at 700 $^{\circ}\text{C}$, (e) annealed at 800 $^{\circ}\text{C}$, (f) after SiO_2 coating of the hematite nanowire, (g) after annealing SiO_2 -coated hematite nanowire at 800 $^{\circ}\text{C}$, and (h) sample seen in panel g after SiO_2 removal.

For an indirect band gap semiconductor, the transition of an electron from the valence to conduction band is phonon-assisted because it involves a change in both energy and momentum.⁷ Indirect band gaps of 2.18 and 2.04 eV were determined for as-prepared and hematite nanowires, respectively, by the Tauc analysis, as shown in Figure 3. These values are comparable to others reported for hematite nanocrystals and films, for example,

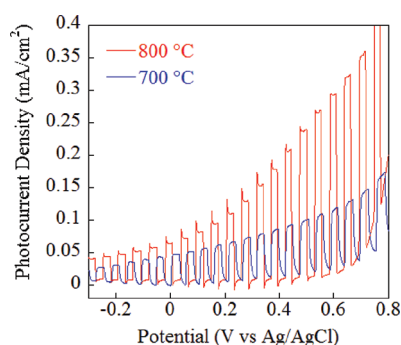


Figure 5. Photocurrent of hematite nanowire arrays annealed at 700 and 800 °C.

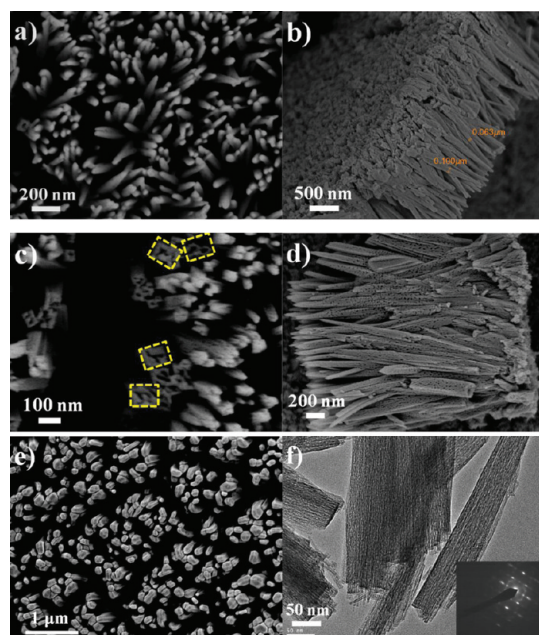


Figure 6. FE-SEM images of hematite nanowire arrays on FTO: (a and b) annealed at 500 °C, (c and d) after SiO₂ treatment, with the yellow dashed line marking the tubular structure, (e) annealed at 820 °C, and (f) TEM image of the as-prepared sample on FTO. The inset is the diffraction pattern.

nanocrystalline hematite made by spray pyrolysis (band gap = 2.05 eV³³) and for iron oxide hydroxide (band gap = 2.12 eV³⁴).

Panels a and b of Figure 4 are SEM images of nanowire arrays grown on Ti foil, annealed at 500 °C in Ar. A negligible photocurrent was observed for this sample, implying unsuccessful doping. After the annealing temperature was increased to 700 °C, the well-shaped wire can still be seen from panels c and d of Figure 4, with a pronounced photocurrent obtained under chopped light, as seen in Figure 5. The Ar annealed nanowires were destroyed at temperatures of 800 °C (see Figure 4e), although no damage was seen for oxygen-annealed samples. To minimize the growth of the hematite feature size during high-temperature annealing, we coated the wires with a layer of SiO₂ before heating, a technique reported by Brillet and co-workers.¹³ Panels f, g, and h of Figure 4 show FE-SEM images of hematite nanowires after SiO₂ coating, annealing at 800 °C, and after the SiO₂ was removed by NaOH, respectively. This approach seems

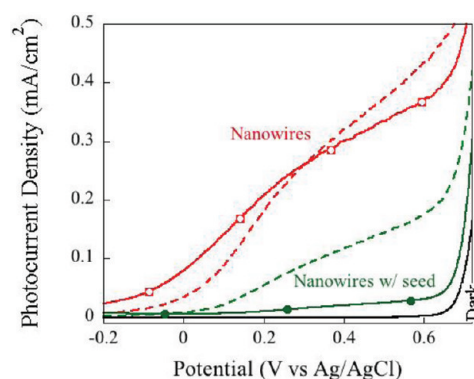


Figure 7. Photocurrent of 1.8 μm long nanowire arrays, with and without seed layers, after two-step annealing at 500/800 °C. The solid curves are obtained under front-side illumination, and the dashed curves are obtained under back-side illumination.

effective for protection of the nanowires, allowing their photoelectrochemical use, as seen in Figure 5.³⁵

No photocurrent was observed for the as-prepared nanowire array films on FTO, and only a very small saturation photocurrent ($\sim 30 \mu\text{A}/\text{cm}^2$) could be seen after annealing at 500 °C. The SEM images of 500 °C annealed samples grown on FTO can be seen from panels a and b of Figure 6. Subsequently, we fabricated a tubular/mesoporous hematite wire arrays by the following procedure: coating as-prepared wires by SiO₂, annealing this wire–SiO₂ composite at 500 °C in air for 5 h, and then removal of silica by NaOH. The similar approach was reported by Hyeon and co-workers to fabricate hematite nanocapsules.³⁶ A tubular structure (marked by a yellow dashed line) can be clearly seen from Figure 6c after the noted SiO₂ treatment, while a mesoporous structure within the wires is also obtained (Figure 6d).

Foundational work^{12,13,28} has been performed toward doping hematite by incorporating Sn from the FTO substrate. However, some critical factors that may affect Sn doping and photoelectrochemical behavior of the resulting hematite nanowire arrays, such as the annealing regime, wire length, grain boundaries, and presence of a seed layer, have not yet been investigated. When the performance of samples was compared with and without seed layers, it was found that the seed layer prevented the electrolyte from contacting the FTO substrate, revealing the existence of gaps between bottoms of the individual wires. However, this seed layer was subsequently found to hinder the temperature-driven diffusion of Sn from the FTO substrate to the hematite nanowires. As shown in Figure 7, the nanowire arrays grown on seed layers show a very low photocurrent under front-side illumination (light incident upon electrolyte, material, FTO, and glass) but a 5-fold increase was observed with back-side illumination (light incident upon glass, FTO, material, and electrolyte) before the onset of the dark current. This suggests that the tops of the nanowires were not effectively doped; thus, the photogenerated charge carriers recombine before they reach the back contact because of low conductivity. In this case, back-side illumination allows the electrons generated close to the FTO surface to be collected efficiently before they recombine with holes,³⁷ with higher photocurrents observed. However, it can clearly be seen that nanowire arrays grown on FTO give rise to a much higher (double) photocurrent than those grown on seed layers, with almost no difference found between front and back illumination. Given the same thickness of the nanowire array films tested, it is

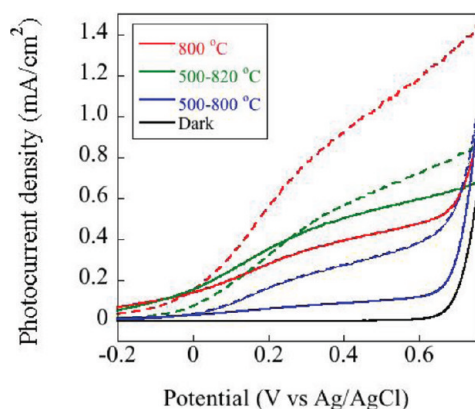


Figure 8. Photocurrent of 2.5 μm long nanowire array films after annealing. The solid curves are obtained under front-side illumination, and the dashed curves are obtained under back-side illumination.

fair to say that the seed layer has a deleterious effect in this doping strategy. To investigate the influence of grain boundaries on the diffusion of Sn from the FTO substrate, a particulate film with the same thickness as the nanowire arrays was prepared.³⁸ The annealed nanoparticle films had photocurrent values comparable to the dark current of the nanowire samples shown in Figure 7; we hypothesize that the grain boundaries between nanoparticles prevent Sn incorporation. However, Sivula et al.^{12,13} have recently reported a mesoporous hematite film prepared by the solution-based colloidal method, with a significantly enhanced photocurrent resulting from Sn doping induced by high-temperature sintering.

For 2.5 μm long nanowires, raising the sintering temperature from 800 to 820 $^{\circ}\text{C}$ greatly increased the photocurrent (see Figure 8), even though the FTO layer become more resistive. The great difference in the photocurrent measured for 800 $^{\circ}\text{C}$ annealing 2.5 μm nanowire array films under front- and back-illumination indicates inefficient Sn doping; in contrast, nanowires shorter than 1.8 μm showed almost no difference with front or back illumination (data not shown). It is noteworthy that all samples with wire lengths between 830 nm and 2.5 μm gave similar photocurrent values before the onset of the dark current when sintered at 820 $^{\circ}\text{C}$, and the illumination direction had little effect. A possible explanation for this is a balance between light absorption and charge transport. Longer wires can absorb more incident photons and offer higher active surface areas, but electrons are lost enroute to the back contact via hole recombination. Short wires reduce the distance of electron transport and recombination, but they absorb less light.

The samples discussed above were first sintered at 500 $^{\circ}\text{C}$ and, then starting from room temperature, heated to the target doping temperature to diffuse Sn from the substrate into the wires. The motivation behind this two-step annealing was to avoid damage to the nanowires; however, we found that higher photocurrent values, $\sim 0.6 \text{ mA}/\text{cm}^2$ at 0.23 V versus Ag/AgCl and $1.3 \text{ mA}/\text{cm}^2$ at 0.7 V versus Ag/AgCl, photocurrent values still lower than Si-doped hematite films,¹¹ could be obtained when the as-prepared nanowire arrays were heated directly to the target temperature, as shown in Figure 8. This photocurrent density is 3 times higher than that of otherwise identical films sintered at 500 $^{\circ}\text{C}$, cooled to ambient temperature, and then heated to 800 $^{\circ}\text{C}$. We hypothesize that Sn diffusion is faster with a more even distribution achieved before the transformation to highly crystalline hematite

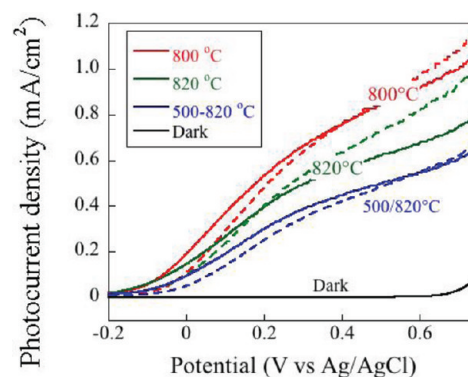


Figure 9. Photocurrent of 830 μm long nanowire array films after annealing. The solid curves are obtained under front-side illumination, and the dashed curves are obtained under back-side illumination.

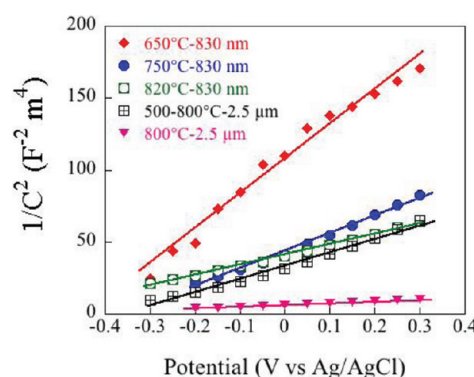


Figure 10. Mott–Schottky plots of hematite nanowire arrays of different lengths and annealing temperatures, obtained in 1 M NaOH (pH 13.6) solutions in the dark.

nanowires takes place. Figure 9 shows the photocurrent response of 830 nm nanowire array films made by both sintering procedures. Heating the sample directly to 820 $^{\circ}\text{C}$ resulted in higher photocurrent values, but the effect was not as pronounced as in the case of longer wires.

To better understand the roles of the sintering temperature and fabrication technique on the electronic properties of hematite nanowire array films, electrochemical impedance spectra were obtained in the dark and under illumination. The flat band potential and donor density determined by Mott–Schottky analysis showed that the estimated flat band potentials (E_{fb}) were -0.43 , -0.35 , and -0.57 V versus Ag/AgCl for 830 nm long nanowire samples directly annealed at 650, 750, and 820 $^{\circ}\text{C}$, respectively (see Figure 10). The flat band potentials E_{fb} for 2.5 μm long wire samples annealed at 800 and 500/800 $^{\circ}\text{C}$ in the two-step procedure were -0.49 and -0.39 V versus Ag/AgCl, respectively. The flat band potentials do not vary monotonically with the doping temperature, but the values obtained are in the range of those found for 4% Ti-doped hematite³⁹ and ultrathin hematite films without doping.⁴⁰ The photocurrent onset potentials measured from the chopped light IV curves (data not shown here) were in agreement with the flat band potentials measured by the Mott–Schottky method, except for the 830 nm wire array annealed at 820 $^{\circ}\text{C}$, where the onset potential was -0.35 V. Although the flat band potential is often assumed to be approximately equal to the onset potential, in many cases, the flat band potential is negative of the photocurrent onset potential, for

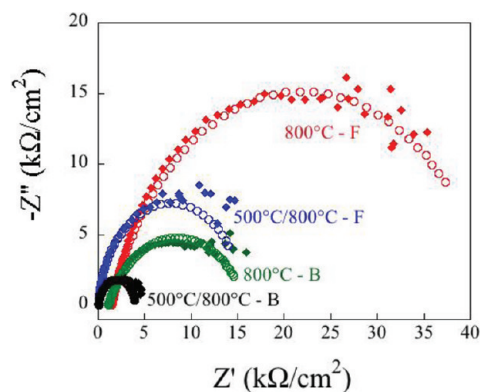


Figure 11. Electrochemical impedance spectra of 2.5 μm long nanowire arrays after annealing, under front-side (F) and back-side (B) illumination, by AM 1.5G light ($100 \text{ mW}/\text{cm}^2$), in 1 M NaOH. Solid diamonds represent experimental data, and open circles represent model values.

example, in the case of Al-doped hematite.⁴¹ The shift is caused by a high recombination rate and slow oxygen evolution kinetics at the hematite surface. Recombination can be suppressed by minimizing recombination centers, such as defects, or by use of surface catalysts that lower the overpotential for oxygen evolution; in either case, the onset potential shifts negative and comes closer to the flat band potential. Similar to our Sn-doped hematite nanowires, Cr- and Mo-doped hematite⁴² also show consistency between the flat band potential and the onset potential. The small changes observed in the flat band potential suggest that the conduction band edge of Fe_2O_3 is not significantly changed by doping.⁴²

The positive slope of the Mott–Schottky plots indicates n-type doping of the nanowire arrays. Using a dielectric constant of 80 for hematite,⁴³ the electron density was estimated to be $7.29 \times 10^{19} \text{ cm}^{-3}$, $1.41 \times 10^{20} \text{ cm}^{-3}$, and $2.45 \times 10^{20} \text{ cm}^{-3}$ for 830 nm long nanowire arrays heated to 650, 750, and 820 $^{\circ}\text{C}$, respectively. The higher donor densities found with samples annealed at higher temperatures is consistent with Sn diffusion from the substrate. These doping densities are comparable to those previously observed for Sn-doped hematite films.²⁸ Most importantly, the 2.5 μm long nanowire arrays annealed at 800 $^{\circ}\text{C}$ gave 1 order of magnitude higher donor density ($1.39 \times 10^{21} \text{ cm}^{-3}$) than those annealed with the 500/800 $^{\circ}\text{C}$ two-step procedure ($1.84 \times 10^{20} \text{ cm}^{-3}$). Two factors may contribute to the higher photocurrents observed at higher doping density. First, increased electrical conductivity of the hematite nanowire arrays leads to faster collection of the majority carriers at the FTO electrode. Second, the increased donor density decreases the thickness of the space charge layer and, consequently, leads to more effective separation and transport of electrons and holes.

Electrochemical impedance spectra of 2.5 μm long nanowire arrays annealed at 800 $^{\circ}\text{C}$ and in the two-step 500/800 $^{\circ}\text{C}$ procedure, measured under illumination by AM 1.5G light ($100 \text{ mW}/\text{cm}^2$), with a 0.5 V bias, are shown in Figure 11. The semicircles for both samples are much larger in the dark than with illumination (Nyquist plots without illumination are not shown here), indicating that the photogenerated charge carriers substantially lower the charge-transfer resistance.⁴⁴ For both samples, back-side illumination gave smaller semicircles than front-side illumination. For low mobility oxide semiconductors, such as hematite, charge carriers produced in the vicinity of the back contact are collected more efficiently,⁴⁵ and this is manifested as a lower resistance in the EIS measurements. This result is consistent with the photocurrent

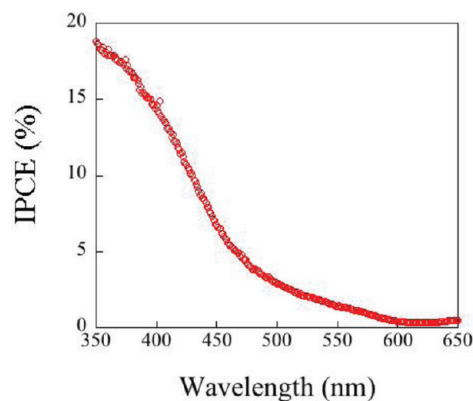


Figure 12. IPCE spectra of a 830 nm long nanowire array film after annealing at 800 $^{\circ}\text{C}$, with a 0.5 V bias, using a two-electrode cell (Pt counter electrode).

measurements that showed higher photocurrent densities with back-side illumination.

Figure 12 shows the IPCE for 830 nm long nanowire arrays annealed at 800 $^{\circ}\text{C}$, measured with a 0.5 V bias. The IPCE drops to zero at wavelengths longer than 600 nm, which is consistent with the hematite band gap. The IPCE was 18% at 352 nm, a value comparable to that of Sn-doped hematite made by high-temperature annealing.²⁸ Undoped arrays of vertically aligned hematite nanorods showed low photoconversion efficiencies,⁴⁵ although the performance can be significantly increased when testing in a 0.1 M KI electrolyte,⁴⁶ and sintered thin films of undoped colloidal hematite gave an IPCE below 1%,⁴⁷ which underscores that doping is essential to improving the photoelectrochemical efficiency of hematite. The n-type Sn doping, such as Ti and Si doping, decreases the series resistance and decreases the width of the depletion layer.

CONCLUSION

Crystalline hematite nanowire arrays with [110] orientation were successfully prepared by an acetonitrile-assisted solvothermal approach. An interesting observation is that a higher acid concentration results in longer nanowires, an affect that may be attributed to the accelerated hydrolysis of acetonitrile. The existence of a substructure comprised of iron oxide hydroxide rods was observed. The annealing procedure, which dopes the nanowires by diffusion of atoms from the underlying substrate, greatly affects the photoelectrochemical properties of the nanowire arrays, with direct heating to 800 $^{\circ}\text{C}$, giving the highest donor density. Further improvement of the hematite nanowire array photoelectrochemical performance might be attained by introducing dopants through other means, because the high-temperature annealing process introduces increased series resistance at the electrode surface. This possibility will be investigated in future experiments.

AUTHOR INFORMATION

Corresponding Author

*E-mail: yangzy@lzu.edu.cn (Z.-Y.Y.); craig.grimes40@gmail.com (C.A.G.).

ACKNOWLEDGMENT

This material is based on work supported as part of the Polymer-Based Materials for Harvesting Solar Energy, an Energy Frontier Research Center funded by the Office of Basic Energy Sciences, Office of Science, U.S. Department of Energy, under Award DE-SC0001087. Dongdong Qin is supported by a scholarship grant from the China Scholarship Council. We thank Dr. O. K. Varghese, S. Friesen, C. N. Henderson, T. H. Wang, E. A. Hernandez-Pagan, Dr. X. J. Feng, and J. Z. Su for their assistance with the work.

REFERENCES

- (1) Fujishima, A.; Honda, K. *Nature* **1972**, 238, 37–38.
- (2) Grätzel, M. *Nature* **2001**, 414, 338–344.
- (3) Khaselev, O.; Turner, J. A. *Science* **1998**, 280, 425–427.
- (4) Sivula, K.; Formal, F. L.; Grätzel, M. *ChemSusChem* **2011**, 4, 432–449.
- (5) Grimes, C. A.; Varghese, O. K.; Ranjan, S. *Light, Water, Hydrogen: The Solar Generation of Hydrogen by Water Photoelectrolysis*; Springer: Berlin, Germany, 2007; Chapter 4, Oxide Semiconducting Materials as Photoanodes.
- (6) Cherepy, N. J.; Liston, D. B.; Lovejoy, J. A.; Deng, H. M.; Zhang, J. Z. *J. Phys. Chem. B* **1998**, 102, 770–776.
- (7) Kennedy, J. H.; Frese, K. W. *J. Electrochem. Soc.* **1978**, 125, 709–714.
- (8) Leland, J. K.; Bard, A. J. *J. Phys. Chem.* **1987**, 91, 5076–5083.
- (9) Dareedwards, M. P.; Goodenough, J. B.; Hamnett, A.; Trelvelick, P. R. *J. Chem. Soc., Faraday Trans. 1* **1983**, 79, 2027–2041.
- (10) Duret, A.; Gratzel, M. *J. Phys. Chem. B* **2005**, 109, 17184–17191.
- (11) Kay, A.; Cesar, I.; Gratzel, M. *J. Am. Chem. Soc.* **2006**, 128, 15714–15721.
- (12) Siula, K.; Zboril, R.; Formal, F. L.; Robert, R.; Weidenkaff, A.; Tucek, J.; Frydrych, J.; Grätzel, M. *J. Am. Chem. Soc.* **2010**, 132, 7436–7444.
- (13) Brillet, J.; Grätzel, M.; Sivula, K. *Nano Lett.* **2010**, 10, 4155–4160.
- (14) Lin, Y. J.; Zhou, S.; Sheehan, S. W.; Wang, D. W. *J. Am. Chem. Soc.* **2011**, 133, 2398–3401.
- (15) Goncalves, R. H.; Lima, B. H. R.; Leite, E. R. *J. Am. Chem. Soc.* **2011**, 133, 6012–6019.
- (16) Chen, J.; Xu, L.; Li, W. Y.; Gou, X. L. *Adv. Mater.* **2005**, 17, 582–586.
- (17) Woo, K.; Lee, H. J.; Ahn, J. P.; Park, Y. S. *Adv. Mater.* **2003**, 15, 1761–1764.
- (18) Wen, X. G.; Wang, S. H.; Ding, Y.; Wang, Z. L.; Yang, S. H. *J. Phys. Chem. B* **2005**, 109, 215–220.
- (19) Jia, C. J.; Sun, L. D.; Luo, F.; Han, X. D.; Heyderman, L. J.; Yan, Z. G.; Yan, C. H.; Zheng, K.; Zhang, Z.; Takano, M.; Hayashi, N.; Eltschka, M.; Kläui, M.; Rüdiger, U.; Kasama, T.; Gontard, L. C.; Dunin-Borkowski, R. E.; Tzvetkov, G.; Raabe, J. *J. Am. Chem. Soc.* **2008**, 130, 16968–16977.
- (20) (a) LaTempa, J. T.; Feng, X. J.; Paulose, M.; Grimes, A. C. *J. Phys. Chem. C* **2009**, 113, 16293–16298. (b) Prakasam, H. E.; Paulose, M.; Varghese, O. K.; Mor, G. K.; Grimes, C. A. *Nanotechnology* **2006**, 17, 4285–4291.
- (21) Mohapatra, S. K.; John, S. E.; Banerjee, S.; Misra, M. *Chem. Mater.* **2009**, 21, 3048–3055.
- (22) Fu, Y. Y.; Wang, R. M.; Xu, J.; Chen, J.; Yan, Y.; Narlikar, A. V.; Zhang, H. *Chem. Phys. Lett.* **2003**, 379, 373–379.
- (23) Liu, J. P.; Li, Y. Y.; Fan, H. J.; Zhu, Z. H.; Jiang, J.; Ding, R. M.; Hu, Y. Y.; Huang, X. T. *Chem. Mater.* **2010**, 22, 212–217.
- (24) Morales, M. P.; Gonzalez-Carreño, T.; Serna, C. J. *J. Mater. Res.* **1992**, 7, 2538–2545.
- (25) Musić, S.; Krehula, S.; Popović, S.; Skoko, Ž. *Mater. Lett.* **2003**, 57, 1096–1102.
- (26) Vayssieres, L.; Beermann, N.; Lindquist, S. E.; Hagfeldt, A. *Chem. Mater.* **2001**, 13, 233–235.
- (27) Peng, L. L.; Xie, T. F.; Fan, Z. Y.; Zhao, Q. D.; Wang, D. J.; Zheng, D. *Chem. Phys. Lett.* **2008**, 459, 159–163.
- (28) Ling, Y.; Wang, G.; Wheeler, D. A.; Zhang, J. Z.; Li, Y. *Nano Lett.* **2011**, 11, 2119–2125.
- (29) Barbosa, L. A. M. M.; Santen, R. A. *J. Catal.* **2000**, 191, 200–217.
- (30) Sze, Y. K.; Irish, D. E. *Can. J. Chem.* **1975**, 53, 427–436.
- (31) Cottineau, T.; Plouet-Richard, M.; Mevellec, J. Y.; Brohan, L. *J. Phys. Chem. C* **2011**, 115, 12269–12274.
- (32) Iordanova, N.; Dupuis, M.; Rosso, K. M. *J. Chem. Phys.* **2005**, 122, No. 144305.
- (33) Akikusa, J.; Khan, S. U. M. *J. Phys. Chem. B* **1999**, 103, 7184–7189.
- (34) Fang, X. L.; Li, Y.; Chen, C.; Kuang, Q.; Gao, X. Z.; Xie, Z. X.; Xie, S. Y.; Huang, R. B.; Zheng, L. S. *Langmuir* **2010**, 26, 2745–2750.
- (35) Zhang, P.; Kleiman-Shwarsstein, A.; Hu, Y. S.; Lefton, J.; Sharma, S.; Forman, A. J.; McFarland, E. *Energy Environ. Sci.* **2011**, 4, 1020–1028.
- (36) Piao, Y.; Kim, J.; Na, H. B.; Kim, D.; Baek, J. S.; Ko, M. K.; Lee, J. H.; Shokouhimenr, M.; Hyeon, T. *Nat. Mater.* **2008**, 7, 242–247.
- (37) Hagfeldt, A.; Björkstén, U.; Lindquist, S. E. *Sol. Energy Mater. Sol. Cells* **1992**, 27, 293–304.
- (38) Bora, D. K.; Braun, A.; Erat, S.; Ariffin, A. K.; Löhnert, R.; Sivula, K.; Töpfer, J.; Grätzel, M.; Manzke, R.; Graule, T.; Constable, E. C. *J. Phys. Chem. C* **2011**, 115, 5619–5625.
- (39) Hahn, N. T.; Mullins, C. B. *Chem. Mater.* **2010**, 22, 6474–6482.
- (40) Klahr, B. M.; Martinson, B. F.; Hamann, T. W. *Langmuir* **2011**, 27, 461–468.
- (41) Kleiman-Shwarsstein, A.; Huda, M. N.; Walsh, A.; Yan, Y.; Stucky, G. D.; Hu, Y. S.; Al-Jassim, M. K.; MacFarland, E. W. *Chem. Mater.* **2010**, 22, 510–517.
- (42) Shwarsstein, A. K.; Hu, Y. S.; Forman, A. J.; Stucky, G. D.; MacFarland, E. W. *J. Phys. Chem. C* **2008**, 112, 15900–15907.
- (43) Cesar, I.; Sivula, K.; Kay, A.; Zboril, R.; Gratzel, M. *J. Phys. Chem. C* **2009**, 113, 772–782.
- (44) Mao, A. M.; Shin, K.; Kim, J. K.; Wang, D. H.; Han, G. Y.; Park, J. H. *ACS Appl. Mater. Interfaces* **2011**, 3, 1852–1858.
- (45) Lindgren, T.; Wang, H. L.; Beermann, N.; Vayssieres, L.; Hagfeldt, A.; Lindquist, S. E. *Sol. Energy Mater. Sol. Cells* **2002**, 71, 231–243.
- (46) Beermann, N.; Vayssieres, L.; Lindquist, S. E.; Hagfeldt, A. *J. Electrochem. Soc.* **2000**, 147, 2456–2461.
- (47) Björkstén, U.; Moser, J.; Gratzel, M. *Chem. Mater.* **1994**, 6, 858–863.